Generalization ability of a CNN γ-ray localization model for radiation imaging

Wei Lu[1] · Hai-Wei Zhang[1] · Ming-Zhe Liu[1] · Hao-Xuan Li[1] · Xian-Guo Tuo[2] · Lei Wang[1,2]

Abstract

In γ-ray imaging, localization of the γ-ray interaction in the scintillator is critical. Convolutional neural network (CNN) techniques are highly promising for improving γ-ray localization. Our study evaluated the generalization capabilities of a CNN localization model with respect to the γ-ray energy and thickness of the crystal. The model maintained a high positional linearity (PL) and spatial resolution for ray energies between 59 and 1460 keV. The PL at the incident surface of the detector was 0.99, and the resolution of the central incident point source ranged between 0.52 and 1.19 mm. In modified uniform redundant array (MURA) imaging systems using a thick crystal, the CNN γ-ray localization model significantly improved the useful field-of-view (UFOV) from 60.32 to 93.44% compared to the classical centroid localization methods. Additionally, the signal-to-noise ratio of the reconstructed images increased from 0.95 to 5.63.

Keywords γ-Ray imaging · γ-Ray localization model · Convolutional neural network · Spatial resolution

1 Introduction

Gamma-ray (γ-ray) imaging can obtain the spatial distribution of γ radioisotopes, which has unique advantages for radioactivity monitoring. This technology is widely used for homeland and public safety, as well as in the nuclear industry, medicine, and other fields. Considering the process of the scintillator detector in γ-ray imaging, the light-field distribution of scintillation generated by the interaction between the rays and scintillators is an essential step that is used to estimate the position of the interaction of the incident γ-rays. Localization algorithms have aimed to expand the useful field-of-view (UFOV) of a crystal, increase the spatial resolution (SR) of the detector, and decrease the

✉ Hai-Wei Zhang
273048544@qq.com

✉ Lei Wang
wl@cdut.edu.cn

[1] Chengdu University of Technology, Chengdu 610059, China

[2] Sichuan University of Science and Engineering, Zigong 643000, China

image distortion caused by hardware nonuniformity [1–4]. Localization algorithms used for γ-imaging mainly include lookup tables, the maximum likelihood, classical center-of-gravity (COG), threshold-center-of-gravity (TCOG), and raise-to-power (RTP) methods [5–7]. The lookup table and maximum likelihood methods significantly improve imaging; however, they require several experiments to obtain the response function of optical photons in the early stage. The COG and TCOG methods have become widely used owing to the availability of rapid computing and simple electronic systems. The COG method estimates the location of interaction by determining the center of gravity of the scintillation light, which can be affected by the light-field shrinkage effect, resulting in a poor resolution at the edge of the image and a reduced UFOV of the detector [8]. Artificial intelligence technology has been used in γ-ray imaging systems.

K-nearest neighbor (KNN) networks have been used to calculate the position of photon interactions in PET and Compton cameras with a resolution of up to 3 mm [9, 10]. However, the long computation time and calibration measurements limit the application of KNN [11]. Feed-forward neural networks (FFNNs), such as the multilayer perceptron (MLP) and radial basis function (RBF), have also been used for γ ray localization [12–18]. Compared to the KNN, the FFNN has a higher SR and can be calculated quickly.

The convolutional neural network (CNN) offers more advantages compared to the FFNN, such as the computing speed and storage scale. The CNN used in radiation imaging has achieved an excellent SR, demonstrating its substantial potential for further development in the nuclear field [19–25].

In a previous study, we developed a gamma imaging system based on monolithic LaBr$_3$(Ce) crystals [26]. Because the transport process of the optical photons inside a LaBr$_3$(Ce) crystal is accurately described, we obtained a response based on the distribution of the scintillation photons and developed the CNN γ-ray localization model. This study investigates the generalization ability of the CNN γ-ray localization model for thick crystals and various energies and establishes an imaging detector model based on the parameters of a physical detector, a CNN γ-ray localization model, and a modified uniform redundant array (MURA) imaging system. The CNN γ-ray localization model significantly weakens the shrinkage effect and improves the signal-to-noise ratio (SNR) of an image in imaging systems using a thick-crystal detector, demonstrating a strong generalization ability over a wide range of γ-ray energies.

2 Materials and methods

Geometry And Tracking 4 (Geant4) and PyTorch were used to build a Monte Carlo detector model, MURA imaging system, and CNN γ-ray localization model. First, we used Geant4 to establish an LaBr$_3$(Ce) detector model based on a physical detector, including accurate electromagnetic and optical processes. Second, a detector response matrix for the neural network dataset was obtained and the CNN model was trained for γ-ray localization using PyTorch. Third, the trained CNN network was used to locate γ rays and the localization results were analyzed.

2.1 Model of imaging detector

In this study, we used Gean4 and PyTorch for the imaging experiments and for training the neural network. The Gean4 simulation code contains the following two systems: flood-field irradiation and MURA imaging. The flood-field irradiation system consists of an imaging detector model and flood-field irradiation, which are used to obtain the dataset for training the neural network and testing the generalization ability of the neural network. The MURA imaging system consists of an imaging detector model, a MURA collimator, and a circular source to test the imaging results of different localization algorithms. Based on PyTorch, we built a CNN γ-ray location model for training the weight parameters and for localization of the interaction points of the rays.

2.1.1 Flood-field irradiation system

The detector model consisted of a monolithic LaBr$_3$(Ce) crystal (51 mm × 51 mm × 5 mm) combined with a silicon photomultiplier (SiPM) array. The 16 × 16 SiPM array (Micro-30035-TSV, ONSEMI) had sensitive and package areas of 3.07 mm × 3.07 mm and 3.16 mm × 3.16 mm, respectively, as shown in Fig. 1a. Teflon (0.3 mm thick) was used as a diffuse reflective layer, which was encapsulated in aluminum foil (0.5 mm) as the reflective mirror layer, and 3 mm of thick glass was at the bottom of the crystal. Optical grease, which was 0.1 mm thick with a reflectivity of 1.41, was used as a light guide for the glass and SiPM array.

Accurate optical processes must be included in the model in addition to physical electromagnetic processes because the detector response must be obtained through the SiPM array. If the wavelength of a photon is significantly greater than the typical atomic spacing, the rays are considered optical photons. In Geant4, optical photons are distinct from high-energy γ photons and are not subject to energy conservation; their energies must not be tallied as part of the balance of a physical event. Electromagnetic and optical processes occur in a detector. The electromagnetic processes include the photoelectric effect, Compton scattering, electron-pair effect, ionization, bremsstrahlung, and multiple scattering. The optical processes include scintillation, Cherenkov radiation, Rayleigh scattering, Mie scattering, bulk absorption, refraction, and reflection [specular spike (SS), specular lobe (SL), Lambertian (L), and backscatter (BS)].

The transport process of optical photons is divided into two categories: the transport process of optical photons inside the material, for which the simulation program requires the user to specify the material parameters, and the transport behavior of optical photons between different media, for which the simulation program requires the specification of the surface parameters. The material parameters control the generation and transport of the optical photons in a material. The surface parameters control the physical processes of the optical photons on the surface between the media. The material parameters mainly refer to the intrinsic parameters of the scintillator, namely, the emission spectrum (EMISSION SPECTRA), light yield (SCINTILLATION YIELD), intrinsic resolution (INTRINSIC RESOLUTION), and time constant (FASTCOMPONENT). The surface parameters mainly include the surface type (TYPE), surface finish (FINISH), detection efficiency (EFFICIENCY), reflectivity (REFLECTIVITY), and reflection type (REFLECTIVITY TYPE).

The transport of optical photons between the boundaries depends on the boundary type (TYPE) of the two dielectric materials. The primary types of boundaries are dielectric–dielectric and dielectric–metal. The dielectric–dielectric boundary is that between two dielectric materials.

(a) Flood-field Irradiation System in Geant4

(b) Mura Image System in Geant4

(c) Structure of CNN in PyTorch
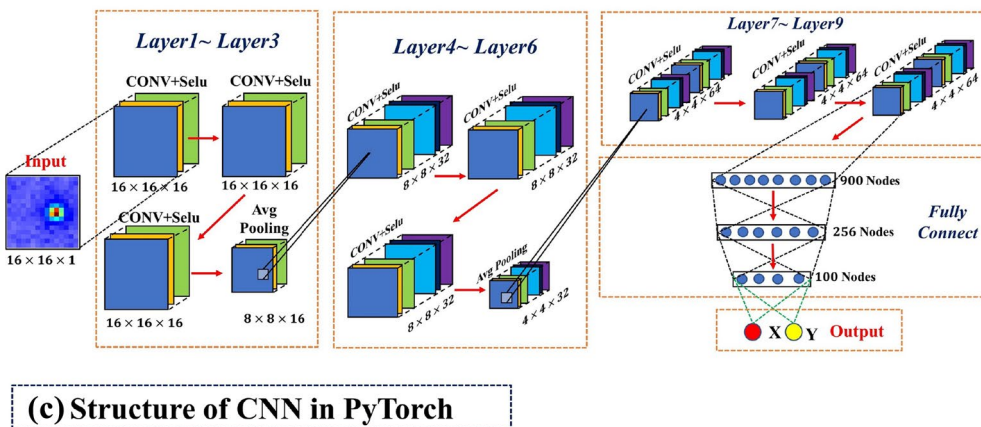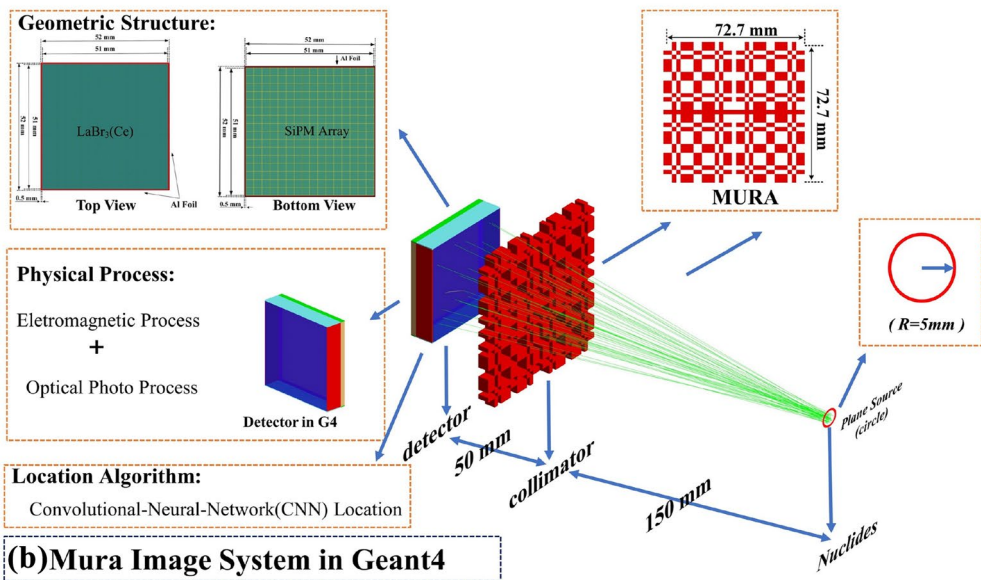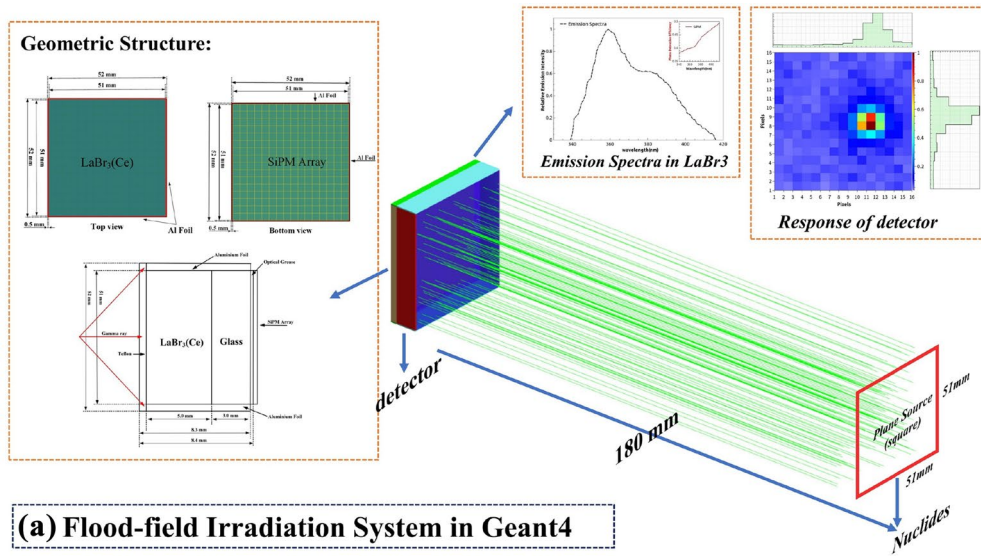
Fig. 1 (Color online) Flood-field irradiation system, MURA imaging system, and CNN structure

Depending on the wavelength of the optical photons, angle of incidence, and refractive index of each dielectric, the optical photons are refracted and reflected by the boundary between the two materials. The dielectric–metal boundary is that between the transparent media and metals. Optical photons can be absorbed by the metal surface or reflected into the transparent media. The absorbance of photons by the metal surface is recorded based on the photon detection efficiency (PDE) of the metal. In this study, the Teflon, SiPM, and LaBr$_3$(Ce) surfaces had dielectric–metal, dielectric–metal, and dielectric–dielectric boundaries, respectively.

During the simulation of the imaging experiment with flood-field irradiation, 122, 365, 662, and 1332 keV γ rays vertically irradiated the incident surface of the detector. When the γ rays interacted with the detector, the detector emitted isotropic scintillation photons at the point of interaction according to the energy that the rays transferred to the detector. For the scintillation photons transported to the surface of the encapsulation material (aluminum foil or Teflon), the total reflection, refraction, or reflection of the photons was simulated according to the wavelength and incident angle of the photons and the refraction coefficients of the materials on either side of the boundary. The scintillation photons reach the SiPM surface and the conversion to electron–hole pairs was determined by the wavelength of the photons and PDE of the SiPM. The number of electron–hole pairs was recorded [24]. The scintillation photons generated during each event were recorded by the SiPM array to form a response matrix, as shown in Fig. 1a. The detector model outputs the corresponding matrix and the two-dimensional coordinates of the incident γ rays for each event. The matrix was normalized and used to train the neural network, and the coordinates were used as labels.

2.1.2 MURA imaging system

Figure 1b demonstrates the MURA imaging system. The MURA-coded aperture collimator in the imaging system was composed of tungsten and was 72.7 mm × 72.7 mm × 5 mm in size. The γ-ray energies emitted from the circular source were as follows: 59 (^{241}Am), 122 (^{57}Co), 59 (^{241}Am), 140 (^{99m}Tc), 365 (^{131}I), 662 (^{137}Cs), 779 (^{152}Eu), 1332 (^{60}Co), and 1460 keV (^{40}K). The distance from the source to the collimator was 180 mm and that from the collimator to the detector surface was 50 mm. The source, coding plate, and detection planes were parallel and coaxial.

During the γ imaging simulation, the rays from the radiation source passed through the collimator, deposited energy in the detector, and emitted scintillation photons. These photons, which were absorbed by the SiPM array after reflection and refraction inside the detector, represent the scintillation distribution and produced a response. Finally, we used several algorithms (CNN, Anger, RTP, TCOG ($\theta = 0.2\%$), TCOG ($\theta = 0.5\%$)) based on the detector response matrix to calculate the coordinates of the position of interaction and counted the events needed to obtain the encoded image. The MELM algorithm was then used to decode the coded image and reconstruct the shape of the radiation source [27].

2.1.3 CNN structure

The CNN was implemented by using PyTorch, which contained nine convolutional layers and three fully connected layers, with two average pooling layers connecting the convolutional layers of different dimensions, as shown in Fig. 1c. In the CNN, the response matrix of each event that was output by the SiPM array was represented by a 16 × 16 tensor input to the CNN. The 2-D coordinates were output following feature extraction by a convolution layer and using fitting calculations by a fully connected layer. The relevant hardware parameters used for developing the CNN are listed in Table 1.

2.2 CNN model training and testing

To improve the generalization ability, 1×10^6 samples (response matrices of events) were used to train the CNN, 2×10^4 samples were used to validate the performance of the CNN and prevent overfitting, and 3.6×10^5 samples were used to test the localization ability. To train the CNN γ-ray localization model, we used 122, 365, 662, and 1332 keV γ rays to vertically irradiate a 5-mm-thick crystal and obtain the response matrices. We used the mean square error (MSE) as

Table 1 Hardware parameters related to CNN

Parameters	Version
Operating System (OS)	Ubuntu 20.04.4 LTS
Graphics Card	NVIDIA GeForce RTX 3080
Central Processing Unit (CPU)	AMD Ryzen Threadripper Pro 3995wx
Integrated Development Environment (IDE)	PyCharm 2020
Deep Learning Frameworks	Pytorch 1.6.0
Computer Programming Language	Python 3.8.3
General Parallel Computing Architectures	Cuda 11.0

the loss function, and the weights of each layer were iteratively updated using the Adam algorithm. The learning rate was set to 1×10^{-4}, and the batch size was 16. The MSE function was defined as follows:

$$\text{MSE} = \frac{\sum_{i=1}^{m} (y^i - \widehat{y}^i)^2}{m} \times D, \tag{1}$$

where i is the sample number, m is the total number of samples, y^i and $\widehat{y}^i$ are the label and predicted values of sample i, respectively, and D is the length of the incident surface of the detector.

The MSEs of the different datasets are listed in Table 2, which range between 0.51 and 0.58; the MSEs of the test and training sets are close, which indicates the strong generalization ability of the CNN.

2.3 Classical localization algorithm

The COG proposed by Anger, which is a classical localization algorithm for γ-imaging, uses the center coordinates of the photoelectric device as linear weights to calculate the position of the interaction of the photon, as expressed by the following:

$$X_{\text{Anger}} = \frac{\sum_{k=1}^{n} x_k c_k}{\sum_{k=1}^{n} c_k}, \tag{2}$$

where X_{Anger} is the coordinate of the incident photon in the x direction, x_k represents the coordinate of the center position of the kth SiPM in the x direction, c_k is the signal collected by the kth SiPM, and n is the number of SiPMs in the x direction. The same equation applies to the y-direction.

The localization results of the COG method demonstrate a strong shrinkage effect in γ-imaging devices owing to the limitations imposed by the nonuniformity of the scintillators and photoelectronic devices [28]. The localization results were compressed toward the center of the image, which reduced the UFOV and enhanced the nonuniformity. Wojcik et al. proposed a truncated center-of-gravity (TCOG) method to reduce the shrinkage effect by setting a threshold [7], where only the signals above the threshold were used to calculate the localization position, whereas those below the threshold were set to zero, as shown in Eq. (3) [8]:

$$X_{\text{TCOG}} = \frac{\sum_{k=1}^{n} x_k \times (c_k - \theta \times c_k)}{\sum_{k=1}^{n} (c_k - \theta \times c_k)}, \tag{3}$$

where θ is the threshold. In this study, $\theta_1 = 0.002$ and $\theta_2 = 0.005$. The same formula is applied in the y-direction. To improve the TCOG method, a raise-to-power (RTP) algorithm was proposed based on the TCOG as follows:

$$X_{\text{RTP}} = \frac{\sum_{k=1}^{n} x_k \times (c_k - \theta \times c_k)^{\alpha}}{\sum_{k=1}^{n} (c_k - \theta \times c_k)^{\alpha}}, \tag{4}$$

where α is a power operation; in this study $\alpha = 2$ and $\theta = 0.005$. The RTP algorithm performs a power operation on the signal; therefore, the position weights are nonlinear. The position weights increase for large signals and decrease for small signals. Thus, the calculated coordinates are near the strong signals [2]. Compared to the TCOG, the RTP algorithm can eliminate the influence of small signals and reduce the shrinkage effect more effectively.

3 Results and discussion

We evaluated the energy generalization ability (EGA) and thickness generalization ability (TGA) of the CNN γ-ray localization model by changing the energy of the rays and thickness of the crystal.

For the EGA evaluation, γ rays of 59, 122, 140, 365, 662, 779, 1332, and 1460 keV were used to test the positional linearity (PL) and spatial resolution (SR). Several localization algorithms, including CNN, Anger, RTP, TCOG ($\theta_1 = 0.002$), and TCOG ($\theta_2 = 0.005$), were employed to evaluate the TGA of the CNN model as well.

3.1 EGA of the CNN γ-ray localization model

The PL represents the deviation of each event measured from the mechanical points; PL is quantified using the L-factor [2] as follows:

$$L = \frac{\Delta X_{\text{measurement}}}{\Delta X_{\text{mechanical}}}, \tag{5}$$

where $\Delta X_{\text{measurement}}$ is the displacement of the measured point, $\Delta X_{\text{mechanical}}$ is the displacement of the mechanical point, and the L-factor is the slope of the linear curve at each measurement point. In a linear graph, the coordinates of the measured and mechanical points follow the $y = \text{slope} \cdot x + \text{intercept}$ relationship, and the PL can be represented by L on the line. In this study, the lower left corner of the detector is considered the origin, and a coordinate system with a minimum scale of 1 mm and a coordinate axis ranging between 0 and 51 mm was established. We step-scanned the detector along the scan path using gamma rays of different energies. In Fig. 3a, the red dotted-line represents the scanning path, the black dots represent the

Table 2 MSE values in different datasets

	Training sets	Validation sets	Test sets
MSE	0.57	0.51	0.58

mechanical points, and the distance between two adjacent mechanical points is 2.5 mm.

The positions of the interaction points of the γ-rays with different energies at each scanning point were calculated by the CNN model. A PL map of the positions of all the mechanical points (2.5 mm step-scanning) was obtained, as shown in Fig. 2b.

The dashed line in Fig. 2b represents the ideal PL curve, where the measured and mechanical points coincide and the slope of the curve is 1. As shown in Fig. 2b, the PL of all the energy rays between the 2.5 and 50 mm range are near the dashed line, and the slopes range between 0.98 and 0.99. The positioning results of the CNN for the rays ranging between 59 and 1460 keV exhibit good PL values. The CNN model demonstrates sufficient EGA values for predicting the position of an interaction point for energies between 59 and 1460 keV.

Figure 3 presents the step scan images of γ-rays with different energies. As shown in Fig. 3b–f, the SR of the mechanical points varied between 0.52 and 0.76 mm when the energy of the γ-rays ranged between 122 and 779 keV.

The SR of the mechanical points varied from 1.05 to 1.19 mm when the γ-ray energy was 59 keV and between 1332 and 1460 keV, as shown in Fig. 3a, g, h. The SR at the mechanical points was considered as the SR of the crystal ($SR_{crystal}$) [22]. The CNN model can accurately locate the position of interaction of the γ-ray with the energy varying from 59 to 1460 keV. The CNN model exhibited a good energy response and strong EGA.

Figure 4 presents the images reconstructed using the MURA system. The circular sources emitting rays of different energies had diameters of 10 mm. The signal-to-noise ratios (SNRs) of the reconstructed images were high, ranging between 5.8 and 15.5 when the ray energies ranged between 59 and 779 keV. When the ray energies were 1332 and 1460 keV, the SNRs of the reconstructed images were 1.0 and 0.84, respectively.

When the energy of the incident ray is low, the cross section of the photoelectric effect is larger than that of the Compton effect, and the collimator can effectively absorb the rays. Hence, the amount of ray scattering is low, and the imaging SNR is high. As the energy increases, the cross
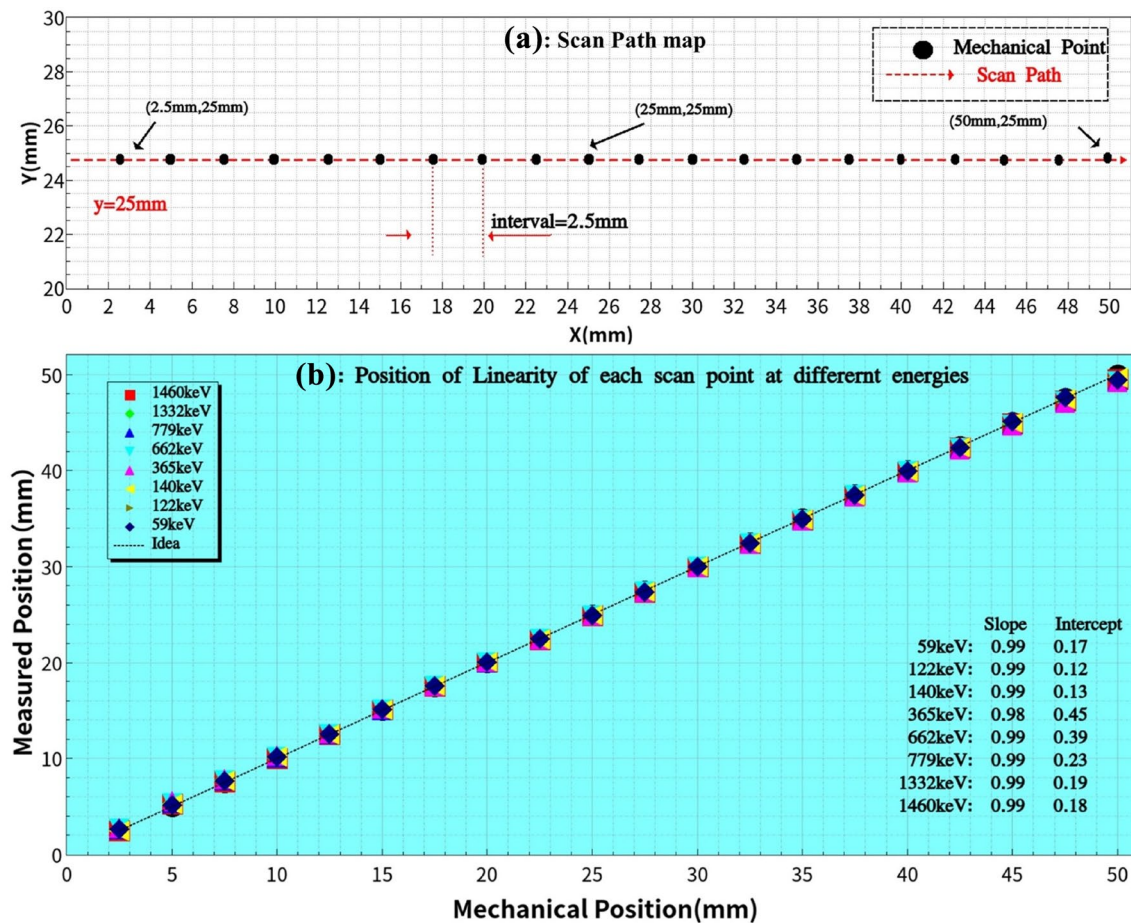
Fig. 2 (Color online) Positional linearity of the mechanical points
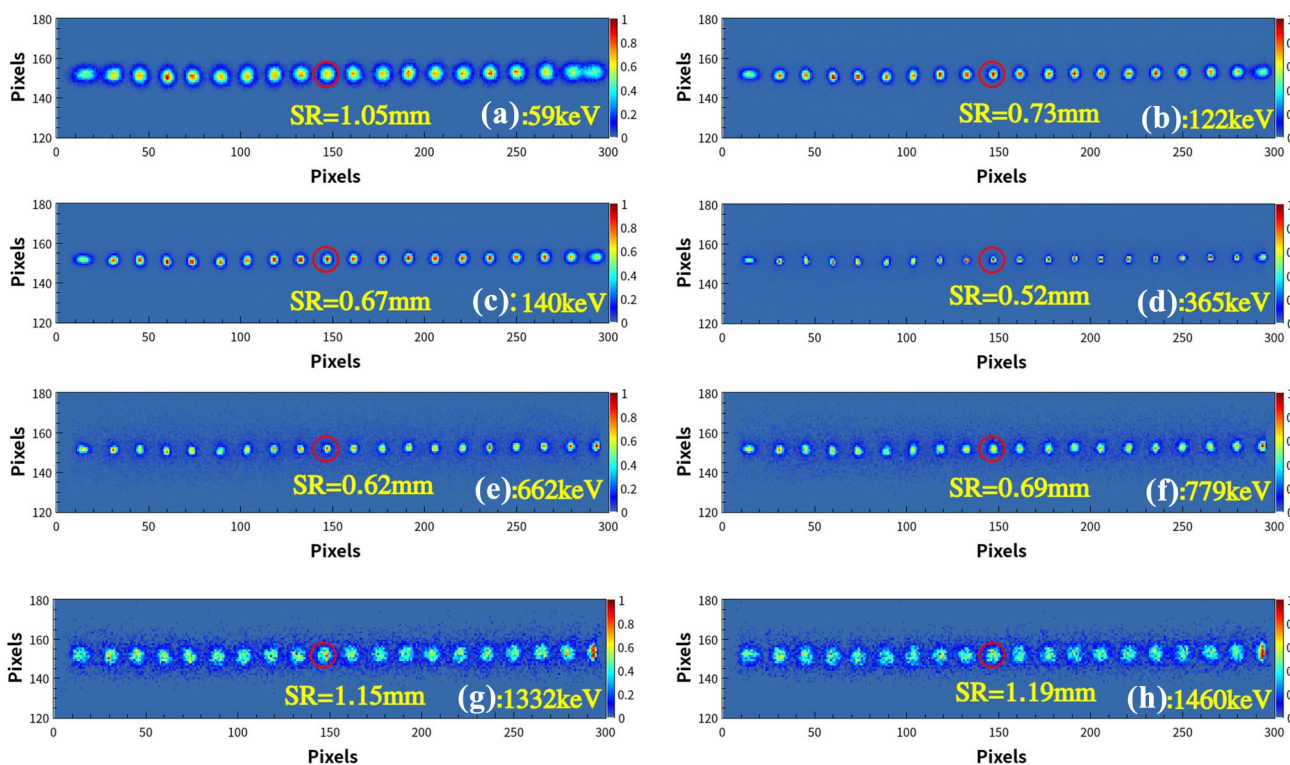
Fig. 3 (Color online) Location of the mechanical points of γ rays with different energies

section of the Compton effect increases. The γ-ray interacts with the MURA-coded aperture collimator, producing several scattered rays that the detector can absorb. The point of interaction between the scattered rays in the detector interferes with the encoded image and decreases the SNR.

In the 1332–1460 keV range, the cross sections of the Compton effect and electron-pair effect continue to increase, and the SNR decreases. This is because the scattered photons generated by multiple scatterings and the electrons generated by the electron-pair effect can change the scintillation light distribution of the detector, affect the accuracy of the CNN positioning, reduce the accuracy of the encoded images, and decrease the SNR. When the energy of the incident γ-ray increases, the MURA-coded aperture collimator cannot effectively absorb the rays, and numerous high-energy rays directly penetrate the collimator and are partly or entirely absorbed by the detector, which significantly disturbs the encoding process and reduces the accuracy of the encoded image.

As shown in Fig. 4i–l, we obtained the reconstructed images by tracking the transport of rays in the model and ignoring the events generated by the Compton scattering rays from the collimator. Compared to Fig. 4e–h of the scattering events, the SNR of the reconstructed image for the 1332 keV rays improved from 1.0 to 5.7, and the SNR of the reconstructed image for the 1460 keV rays improved from

0.84 to 5.0. This indicates that the scattered high-energy rays significantly affect the SNR of the reconstructed image. The influence of scattered rays in a γ-ray imaging system should be considered. The thickness and material of the collimator significantly impact the absorption of rays, notably affecting the imaging quality.

In addition to the E_γ of the incident ray, the imaging resolution $SR_{detector}$ of the MURA system is related to the detector resolution $SR_{crystal}$ and collimator resolution $SR_{collimator}$, as shown in Eq. (6) [29]:

$$(SR_{detector})^2 = (SR_{collimator})^2 + (SR_{crystal})^2. \qquad (6)$$

The energy of the rays and the $SR_{crystal}$ are the main factors influencing the resolution of the MURA imaging system. We calculated the relative error (R) of the diameter in the reconstructed source ($D_{reconstructed}$) and simulated a source ($D_{simulated}$) using Eq. (7) to evaluate the $SR_{detector}$ of the MURA imaging system, as listed in Table 1.

$$R = \frac{D_{reconstructed}}{D_{simulated}} \times 100\%. \qquad (7)$$

As shown in Table 3, compared to the 365 keV γ-ray, the SR of the crystal is greater than 1 mm when the energy of the γ-ray is 59 keV, and a poorer SR of the system leads to a larger relative geometric error of the radioactive source
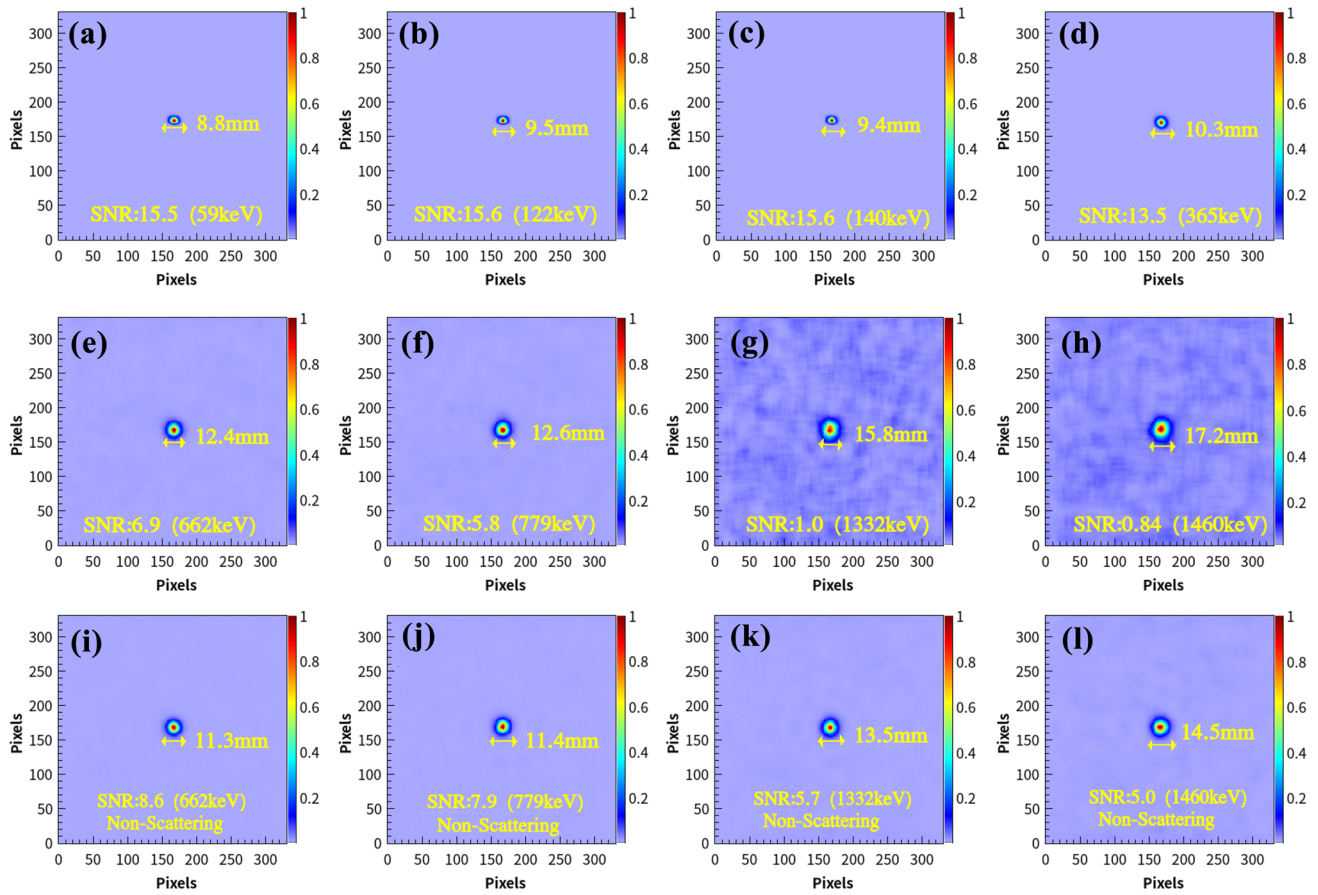
Fig. 4 (Color online) Reconstruction of circular γ-ray source, with and without scattering

Table 3 Relative error in the diameters of the reconstructed and simulated sources

E_γ (KeV)	$SR_{crystal}$ (mm)	$D_{reconstruted}$ (mm)	$D_{simulated}$ (mm)	R (%)
59	1.05	8.8	10	−12
122	0.73	9.5	10	−5
140	0.67	9.4	10	−6
365	0.52	10.3	10	+3
662	0.62	12.4	10	+24
779	0.69	12.6	10	+26
1332	1.15	15.8	10	+58
1460	1.19	17.5	10	+75

in the reconstructed image. When the energy of the γ-ray ranges between 122 and 365 keV, the collimator effectively absorbs the incident ray; however, the SR of the crystal is also high. Consequently, the relative error of the diameter of the circular source in the reconstructed image is the smallest. When the energies of the rays range between 662 and 1460 keV, the γ- and scattered rays are directly absorbed by the detector owing to the high energy, which strongly affects the projected image; therefore, the relative error of the reconstructed image increases as the energy of the radiation increases.

Although only four types of γ rays were used to train the CNN γ-ray localization model in this study, the model can accurately locate rays of unknown energies ranging between 59 and 1460 keV with a good PL and SR, indicating that the CNN γ-ray localization model demonstrates good localization and EGA characteristics. A MURA imaging system based on a neural network model can reconstruct the shape of a radiation source with energies ranging between 59 and 1460 keV, which indicates that this localization method can be easily applied to imaging systems.

3.2 Thickness generalization ability of the CNN γ-ray localization model

We applied the CNN γ-ray localization model to crystals that were 5 and 10 mm thick. The PL and SR of the mechanical points were calculated to evaluate the thickness generalization ability of the model. In addition to the CNN γ-ray

localization model, we used TCOG-0.002, TCOG-0.005, RTP, and Anger for comparison.

The PL of the mechanical points was calculated as shown in Fig. 5a, b. When the thickness of the crystal was 5 mm, the PL values of the CNN, RTP, and TCOG-0.005 were

higher than those of TCOG-0.002 and Anger. When the thickness of the crystal increased to 10 mm, the slopes of RTP, TCOG-0.005, and TCOG-0.002 algorithms decreased from 0.97 to 0.92, 0.94 to 0.92, and 0.42 to 0.38, respectively. Furthermore, the slope of the Anger algorithm decreased
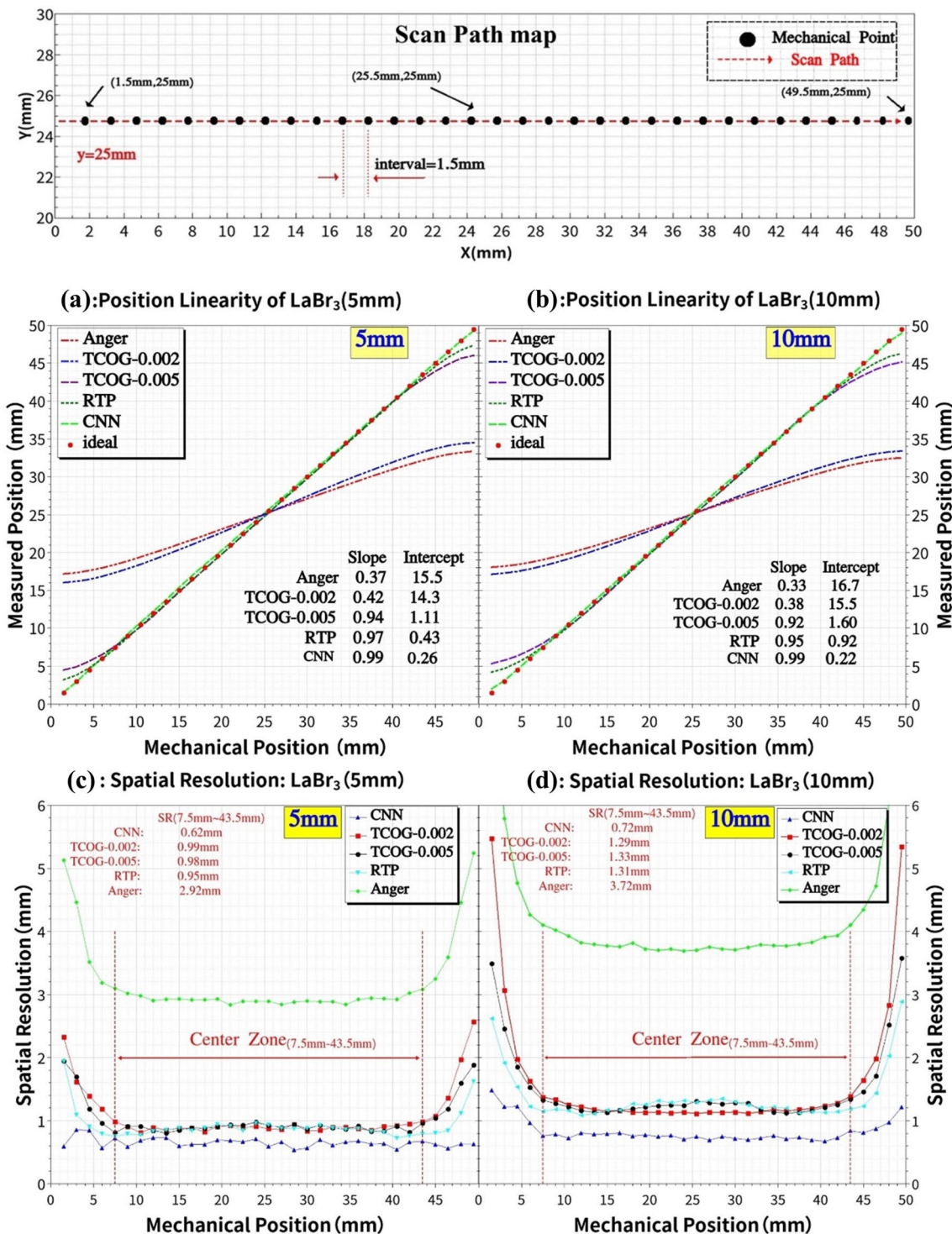
Fig. 5 (Color online) The PL and SR of the mechanical points in crystals that are 5 and 10 mm thick

from 0.37 to 0.33, whereas that of the CNN remained nearly unchanged. By comparing Fig. 5a, b, the CNN model apparently has the best PL for the same thickness, and under the same localization algorithm, the PL of a thick crystal is worse than that of a thin crystal. This is because the shrinkage effect increases as the thickness of the crystal increases; therefore, the range of the light distribution changes as the thickness of the crystal changes, which decreases the localization ability of the traditional algorithm. In contrast, the CNN γ-ray localization model can reduce shrinkage and maintain a high PL in thick crystal detectors.

The SR of the scanned points at different thicknesses are shown in Fig. 5c, d. As shown in Fig. 5c, the SRs of the four algorithms based on the Anger localization method were not significantly different at the central region for the same thickness of the crystal. At the edge, the spatial resolution of the CNN γ-ray localization model is higher than Anger because it can better reduce the shrinkage effect. Using the same thickness of the crystal, the CNN γ-ray localization model obtained a better SR at both the center and edge, where the accuracy determined was significantly higher than that obtained by using other algorithms.

Comparing Fig. 5c, d, for the same localization algorithm, the shrinkage effect caused by the boundary reflection layer becomes increasingly evident owing to the increase in the thickness of the crystal, and finally deteriorates the SR. As the thickness of the crystal increases from 5 to 10 mm, the SR values obtained by using the Anger, TCOG-0.002, TCOG-0.005, RTP, and CNN methods decrease from 2.92 to 3.72 mm, 0.99 to 1.29 mm, 0.98 to 1.33 mm, 0.95 to 1.31 mm, and 0.62 to 0.72 mm, respectively. Compared to the Anger method and its related algorithms, the decrease in the SR of the CNN is lower and is less affected by the shrinkage effect.

Although we trained the CNN model based on the data of a crystal that was 5 mm thick, the CNN can predict the interaction positions of the rays in a crystal with a thickness of 10 mm, which indicates that in addition to the CNN model being used for thick crystals, it can also be used for a strong TGA.

A high positional linearity is significantly helpful for obtaining a large UFOV and high SR. The proposed CNN γ-ray localization model with a high PL can accurately obtain the position of an incident ray, including at the edges, instead of being compressed to the center, which can significantly reduce the shrinkage effect, thus improving both the spatial resolution and UFOV.

The UFOVs of the detector with crystals that were 5 and 10 mm thick were calculated using different algorithms, as shown in Fig. 6. The CNN γ-ray localization model presents the largest UFOV, whereas that of the Anger algorithm is the smallest at the same thickness. As shown in Fig. 6a3–a5, the UFOV of the CNN γ-ray localization model increased by 26.48 and 17.83% compared to the UFOV of TCOG-0.002 and TCOG-0.005, respectively, indicating that the CNN γ-ray localization model effectively improved the UFOV of the detector.

Compared to other algorithms, the edges of the images were less affected by the shrinkage effect when using the CNN γ-ray localization model, and the vertex and center counts were significantly close, indicating that the uniformity was significantly improved. Compared to the 5 mm crystal, the UFOV obtained by RTP and TCOG-0.005 in the 10 mm crystal detector decreased by 10.24 and 9.77%, respectively, while that of the CNN model decreased by 3.60%. This demonstrates that the CNN γ-ray localization model can more effectively reduce the influence caused by the shrinkage effect.
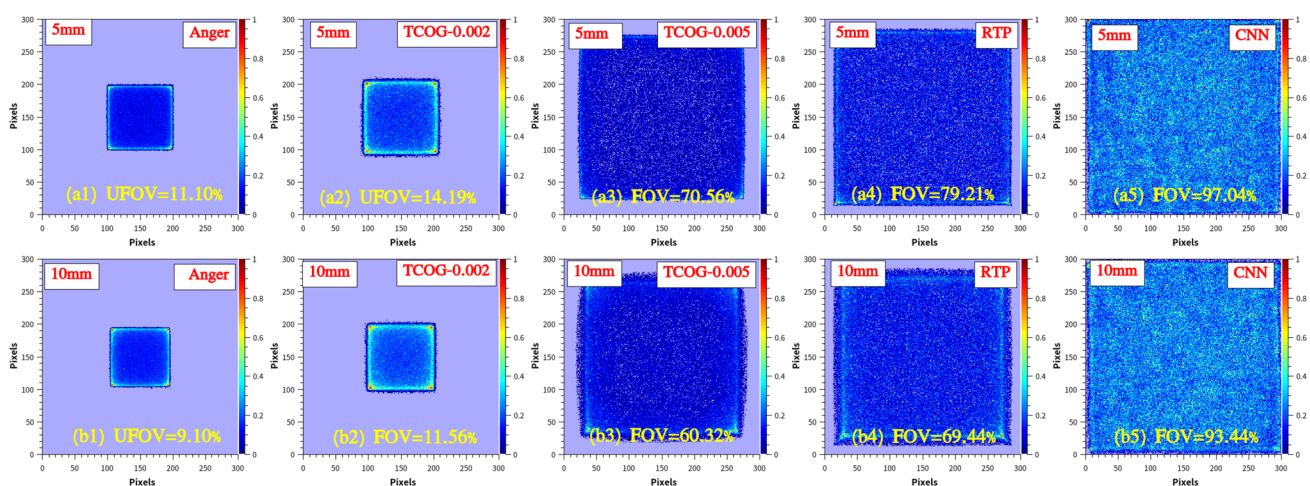
Fig. 6 (Color online) UFOV of crystals that are 5 and 10 mm thick under different algorithms

Figure 7 presents the reconstructed images of a circular source (6 mm in diameter) obtained by using a detector with crystals of two different thicknesses.

As shown in Fig. 7a1, a2, for the detector with the 5 mm crystal, the UFOV area is significantly small for the collimator to obtain a full projection on the detector because the Anger and TCOG-0.002 algorithms are severely affected by the shrinkage effect. Therefore, imaging systems based on these two algorithms cannot reconstruct radioactive sources. As shown in Fig. 6a3–a5, the UFOVs calculated by TCOG-0.005, RTP, and the CNN γ-ray localization model are 70.56, 79.21, and 97.04%, respectively; these three algorithms have a relatively large UFOV. Therefore, the complete projection obtained by the MURA collimator is available in the encoded image of the detector and can image the circular source, as shown in Fig. 7a3–a5. Regarding image quality, the CNN γ-ray localization model has a better PL and less distortion and aberration in the MURA-projected image compared to TCOG-0.005 and RTP, thus the CNN-based reconstructed image has the highest SNR. Considering the shape of the circular source in the reconstructed image, the CNN-based reconstructed image presents the smallest error among the three algorithms in its diameter, which is because the CNN γ-ray localization model has the highest SR and smallest error in the projected image, which indirectly reduces the error in the circular source of the reconstructed image.

As shown in Fig. 7b1–b5, when the thickness of the crystal increased to 10 mm, the shrinkage effect reduced the accuracy of the localization algorithm and increased the distortion of the MURA projection. In addition to the CNN γ-ray localization model, imaging systems based on other algorithms cannot perform image reconstruction on

the ray source. Considering the 10 mm crystals, only the CNN γ-ray localization model can effectively reduce the shrinkage effect on the reconstructed image and reconstruct the image with a high SNR and small error in the diameter of the circular source. The imaging results demonstrate that the detector can be used with thick crystals in the MURA imaging system if the CNN γ-ray localization model is used.

3.3 Advantages of the CNN localization model

Compared to classical algorithms, the CNN γ-ray localization model proposed in this study has the following two advantages.

First, because the CNN γ-ray localization model can effectively improve the PL and SR of the detector, the CNN can significantly improve the UFOV of the detector. In a MURA imaging system, a larger UFOV can increase the integrity of the projected image, increase the SNR of the reconstructed image, and reduce reconstruction errors.

Second, the CNN γ-ray localization model can effectively reduce the impact of the shrinkage effect, thus it has a strong EGA and thickness generalization ability. The EGA of the CNN γ-ray localization model can enable the imaging system to have wide-energy imaging capabilities, and the thickness generalization energy enables the imaging system to use thick crystals for imaging. Classical γ cameras use thin crystals to avoid image distortion and aberrations caused by shrinkage effects, thus resulting in lower detection efficiency, poor energy resolution, and longer imaging time. The CNN γ-ray localization model can be used with crystals having a larger thickness to overcome the shortcomings of thin crystals.
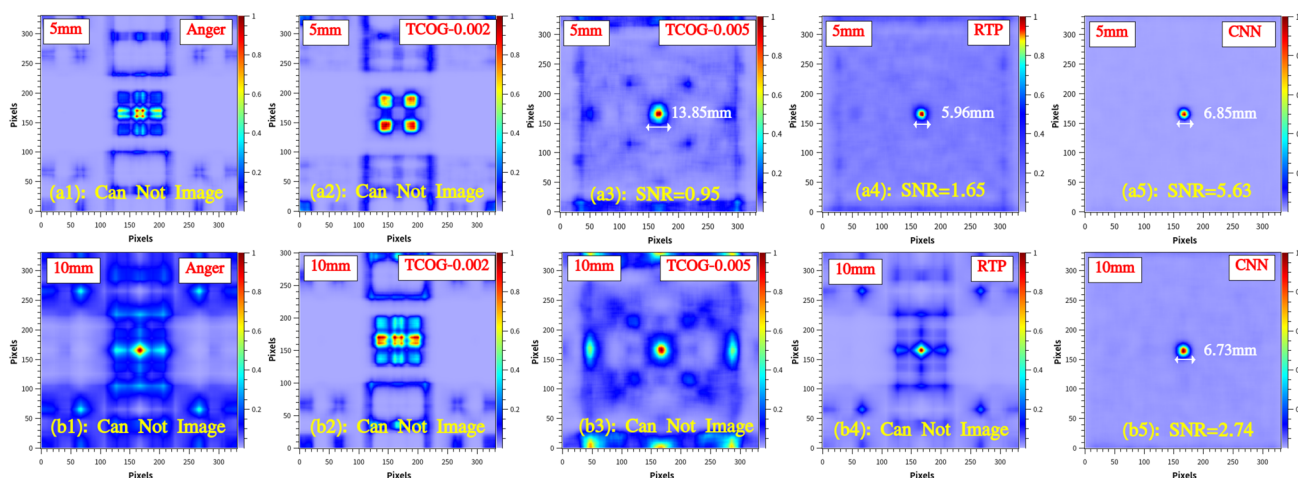
Fig. 7 (Color online) MURA imaging results obtained by using different algorithms for the 5 and 10 mm crystals

4 Conclusion

This study evaluated the generalization ability of the CNN γ-ray localization model for the energy of incident γ rays and the thickness of the detector crystal. We used the CNN γ-ray localization model to predict the interaction positions of the γ-rays with energies ranging between 59 and 1460 keV in the detector crystal and obtained high PL (0.98–0.99) and SR (0.52–1.19 mm) values. The CNN γ-ray localization model can effectively enhance the positional linearity and improve the UFOV of the imaging system. Compared to the classical Anger algorithm, the UFOV can be improved from approximately 10% to greater than 90%. The SR of the edge of the detector was effectively improved and remained consistent with the central region by using the CNN γ-ray localization model.

Moreover, the imaging performance of the MURA system using the CNN model was significantly improved, and the SNR of the reconstructed images was 5.92 times greater than the TCOG-0.005 algorithm. The CNN γ-ray localization model demonstrated significant generalization capabilities of the energy and thickness of the crystal in imaging systems with thick continuous crystals. The SNR of the images was significantly improved, demonstrating significant development potential.

Declarations

References

1. R. Pani, R. Pellegrini, P. Bennati, Investigation on a small FoV γ camera based on LaBr$_3$(Ce):Ce continuous crystal. Nucl. Phys. B **197**, 202–205 (2009). https://doi.org/10.1016/j.nuclphysbps.2009.10.067

2. R. Pani, M. Bettiol, E. Preziosi et al., Position algorithm for monolithic scintillation crystals based on charge projection readout. J. Instrum. **11**, C01061 (2016). https://doi.org/10.1088/1748-0221/11/01/C01061

3. M. Mikeli, A. Polychronopoulou, A. Gektin et al., A new position reconstruction method for position sensitive photomultipliers, in *IEEE Nuclear Science Symposium Conference Record* (2008), pp. 4736–4741. https://doi.org/10.1109/NSSMIC.2008.4774303

4. A. Fabbri, D. Sacco, P. Bennati et al., Study of position reconstruction of a LaBr$_3$(Ce):Ce continuous scintillation crystal for medical applications. J. Instrum. **8**, P12010 (2013). https://doi.org/10.1088/1748-0221/8/12/P12010

5. J. Gen, D.W. Jie, W.X. Tao et al., Position calibration system for imaging detector based on flat plate scintillation crystal. Atom Energy Sci. Technol. **50**, 2055–2059 (2016). https://doi.org/10.7532/yzk.2016.50.11.2055. (**in Chinese**)

6. C.W. Lerche, A. Ros, J.M. Monzó et al., Maximum likelihood positioning for γ-ray imaging detectors with depth of interaction measurement. Nucl. Instrum. Methods Phys. Res. **604**, 359–362 (2009). https://doi.org/10.1016/j.nima.2009.01.060

7. R. Wojcik, S. Majewski, B. Kross et al., High spatial resolution γ imaging detector based on a 5″ diameter R3292 Hamamatsu PSPMT. IEEE Trans. Nucl. Sci. **45**, 487–491 (1998). https://doi.org/10.1109/23.682432

8. R.G. Shi, Y.J. He, Y. Chen et al., Design of a γ camera based on LaBr$_3$(Ce) scintillator array. Nucl. Electron. Detect. Technol. **39**, 22–25 (2019). https://doi.org/10.3969/j.issn.0258-0934.2019.01.006. (**in Chinese**)

9. D.R. Schaart, H. Dam, S. Seifert et al., A novel, SiPM-array-based, monolithic scintillator detector for PET. Phys. Med. Biol. **54**, 3501–3512 (2009). https://doi.org/10.1088/0031-9155/54/11/015

10. S. Liprandi, M. Mayerhofer, S. Aldawood et al., Sub-3mm spatial resolution from a large monolithic LaBr$_3$(Ce) scintillator. Curr Dir. Biomed. Eng. **3**, 655–659 (2017). https://doi.org/10.1515/cdbme-2017-0138

11. H.T. Van, S. Seifert, R. Vinke et al., Improved nearest neighbor methods for γ photon interaction position determination in monolithic scintillator PET detectors. IEEE Trans. Nucl. Sci. **58**, 2139–2147 (2011). https://doi.org/10.1109/TNS.2011.2150762

12. Y. Wang, W. Zhu, X. Cheng et al., 3D position estimation using an artificial neural network for a continuous scintillator PET detector. Phys. Med. Biol. **58**, 1375 (2013). https://doi.org/10.1088/0031-9155/58/5/1375

13. A. Sanaat, H. Zaidi, Depth of interaction estimation in a preclinical PET scanner equipped with monolithic crystals coupled to SiPMs using a deep neural network. Appl. Sci. **10**, 4753 (2020). https://doi.org/10.3390/APP10144753

14. R.J. Aliaga, J.D. Martinez, R. Gadea et al., Corrected position estimation in PET detector modules with multi-anode PMTs using neural networks. IEEE Trans. Nucl. Sci. **53**, 776–783 (2005). https://doi.org/10.1109/TNS.2006.875438

15. V. Babiano, L. Caballero, D. Calvo et al., γ-Ray position reconstruction in large monolithic LaCl$_3$(Ce) crystals with SiPM readout. Nucl. Instrum. Methods A **931**, 1–22 (2019). https://doi.org/10.1016/j.nima.2019.03.079

16. P. Bruyndonckx, S. Léonard, S. Tavernier et al., Neural network-based position estimators for PET detectors using monolithic LSO blocks. IEEE Trans. Nucl. Sci. **51**, 2520–2525 (2004). https://doi.org/10.1109/TNS.2004.835782

17. I. Ladarescu, V. Babiano, J. Balibrea, et al., γ-Ray position reconstruction in large lanthanum-halide crystals with SiPM readout: analytical vs. neural-network algorithms, in *2019 IEEE Nuclear Science Symposium and Medical Imaging Conference (NSS/MIC)* (Manchester, 2019), pp. 1–5. https://doi.org/10.1109/NSS/MIC42101.2019.9059754

18. A. Sanaat, H. Zaidi, Accurate estimation of depth of interaction in PET on monolithic crystal coupled to SiPMs using a deep neural network and Monte Carlo simulations, in *2019 IEEE Nuclear Science Symposium and Medical Imaging Conference (NSS/MIC)* (Manchester, 2019), pp. 1–3. https://doi.org/10.1109/NSS/MIC42101.2019.9059782

19. A. Labella, P. Vaska, W. Zhao et al., Shallow convolutional neural network for 3D γ ray localization in high resolution PET, in *2019 IEEE Nuclear Science Symposium and Medical Imaging Conference (NSS/MIC)* (Manchester, 2019), pp. 1–4. https://doi.org/10.1109/NSS/MIC42101.2019.9059668

20. M. Kawula, T.M. Binder, S. Liprandi et al., Sub-millimeter precise photon interaction position determination in large monolithic scintillators via convolutional neural network algorithms. Phys. Med. Biol. **66**, 135017 (2021). https://doi.org/10.1088/1361-6560/ac06e2

21. L. Tao, X. Li, L.R. Furenlid et al., Deep learning based methods for γ ray interaction location estimation in monolithic scintillation crystal detectors. Phys. Med. Biol. **65**, 115007 (2020). https://doi.org/10.1088/1361-6560/ab857a

22. W. He, Y. Wang, X. Liang et al., High-performance coded aperture γ camera based on monolithic GAGG: Ce crystal. Rev. Sci. Instrum. **92**, 013106 (2021). https://doi.org/10.1063/5.0035991

23. X. Li, M. Ruiz-Gonzalez, L.R. Furenlid, An edge-readout, multilayer detector for positron emission tomography. Med. Phys. **45**, 2425–2437 (2018). https://doi.org/10.1002/mp.12906

24. L.Y. Zhou, H. Zha, J.R. Shi et al., A non-invasive diagnostic method of cavity detuning based on a convolutional neural network. Nucl. Sci. Tech. **33**, 94 (2022). https://doi.org/10.1007/s41365-022-01069-z

25. X.Y. Guo, L. Zhang, Y.X. Xing, Study on analytical noise propagation in convolutional neural network methods used in computed tomography imaging. Nucl. Sci. Tech. **33**, 77 (2022). https://doi.org/10.1007/s41365-022-01057-3

26. W. Lu, L. Wang, Y. Yuan et al., Monte Carlo simulation for performance evaluation of detector model with a monolithic $LaBr_3(Ce)$ crystal and SiPM array for γ radiation imaging. Nucl. Sci. Tech. **33**, 107 (2022). https://doi.org/10.1007/s41365-022-01081-3

27. T. Zhang, L. Wang, J. Ning et al., Simulation of an imaging system for internal contamination of lungs using MPA-MURA coded aperture collimator. Nucl. Sci. Tech. **32**, 17 (2021). https://doi.org/10.1007/s41365-021-00849-3

28. Q.S. Dai, C.L. Zhao, Y.J. Qi, A cost-effective design of compact γ camera module based on continuous crystal. Nucl. Tech. **33**, 54–58 (2010). (**in Chinese**)

29. C. Simon, S. James, P. Michael et al., *Physics in Nuclear Medicine*, vol. 14, 4th edn. (2012), pp. 224–225. https://doi.org/10.1016/B978-1-4160-5198-5.00014-9